Journal of Electrochemical Energy Conversion and Storage. Received October 03, 2025;
Accepted manuscript posted January 19, 2026. doi:10.1115/1.4070915

Stabilizing Cathode–Electrolyte Interphase of Nickel-Rich Single-Crystal Cathodes for Lithium-Ion Batteries

Collin Farrell,[1] Marm Dixit,[1] Molleigh Preefer,[2] Ritu Sahore,[3] Saiful M. Islam,[4] Subrata Chandra Roy,[4] Mengya Li*[1]

1 Electrification and Energy Infrastructure Division, Oak Ridge National Laboratory, Oak Ridge, Tennessee 37831, USA

2 Stanford Synchrotron Radiation Lightsource, SLAC National Accelerator Laboratory, Menlo Park, CA 94025, USA

3 Chemical Sciences Division, Oak Ridge National Laboratory, Oak Ridge, Tennessee 37830, USA

4 Department of Chemistry, Physics, and Atmospheric Sciences, Jackson State University, Jackson, Mississippi 39217, USA

***Corresponding author:**

Mengya Li (lim1@ornl.gov)

Journal of Electrochemical Energy Conversion and Storage. Received October 03, 2025;
Accepted manuscript posted January 19, 2026. doi:10.1115/1.4070915

ABSTRACT

Nickel-rich single-crystal (SC) layered oxides are promising cathode candidates for next-generation lithium-ion batteries (LIBs) owing to their high energy density and structural robustness against intergranular cracking. However, their intrinsic surface reactivity with liquid electrolytes accelerates parasitic reactions at the cathode–electrolyte interphase (CEI), leading to transition-metal dissolution, gas generation, and impedance buildup. In this work, we synthesized SC-$Li_xNi_{0.9}Mn_{0.05}Co_{0.05}O_2$ (NMC9055, $1 \leq x \leq 1.2$) using a eutectic-assisted method and investigated interface stabilization strategies. A nickel-deficient $Li_xNi_{0.6}Mn_{0.2}Co_{0.2}O_2$ (NMC622, $1 \leq x \leq 1.2$) coating was applied via evaporation-based deposition to suppress CEI degradation pathways. Structural and compositional analyses confirmed uniform shell formation and preserved particle integrity. Half-cell electrochemical testing against lithium metal revealed ~10% higher capacity retention and improved reversibility compared with pristine SC NMC9055, particularly under high-voltage operation. These results highlight the critical role of controlled surface chemistry in mitigating CEI instability in nickel-rich SC cathodes, offering a pathway toward enabling durable high-energy LIBs.

Journal of Electrochemical Energy Conversion and Storage. Received October 03, 2025;
Accepted manuscript posted January 19, 2026. doi:10.1115/1.4070915

INTRODUCTION

The global demand for high-performance rechargeable batteries, driven largely by the electrification of transportation, has accelerated research and development (R&D) on lithium-ion batteries (LIBs).[1-3] Early commercial LIBs, which typically employed lithium cobalt oxide (LCO) cathodes paired with graphite anodes, demonstrated excellent reliability in portable electronics in the early 2000s.[4] These cells delivered a practical full-cell capacity of ~140 mAh g^{-1} with favorable thermal stability, and LCO remains widely utilized in smaller electronic devices.[5, 6] At larger scales, however, LCO-based batteries become cost-prohibitive and prone to structural degradation. The advent of nickel manganese cobalt oxide (NMC) cathodes in the early 2000s ushered in a new generation of LIBs, offering reduced cost and improved performance, enabled by advances in mining, purification, and large-scale synthesis.[7] Since their introduction into the battery electric vehicle (BEV) market, the demand for NMC materials has risen exponentially, particularly in the 2020s following Tesla's commercialization of the 2170 and 4680 cells manufactured by Panasonic.[8, 9] R&D efforts have since shifted from NMC111 toward progressively Ni-rich compositions (e.g., NMC532, NMC622, and NMC811) to increase energy density and meet the growing demand for extended driving ranges.[10-17] Nonetheless, further improvements in cycle life and safety are critical to address the practical requirements of both electric vehicles (EVs) and grid-scale energy storage. Among all cell components, the cathode exerts the most significant influence on capacity and cycling stability. With theoretical capacities around half that of their graphite anode counterparts, and the myriad of chemical reactions that occur inside the cathode and at the electrolyte interface, improving cathode material has the potential to make significant impact on cell performance.[18-20]

Journal of Electrochemical Energy Conversion and Storage. Received October 03, 2025;
Accepted manuscript posted January 19, 2026. doi:10.1115/1.4070915

Commercial NMC particles are typically manufactured as spherical secondary particles to maximize packing density. However, a major drawback of polycrystalline (PC) NMC is the progressive loss of capacity during long term cycling. This degradation is primarily driven by the Jahn–Teller effect, which induces localized oxidation state changes within the crystal structure and generates internal stresses. Over extended cycling, these stresses cause fractures along grain boundaries within the spherical particles, as demonstrated by Tanim et al.[15] The resulting fractures enlarge the interfacial area between the active material and the surrounding electrolyte. Such increased interfacial contact area accelerates parasitic reactions at the cathode/electrolyte interface (CEI), producing unwanted gases and forming resistive interphases that hinder, thereby reducing the stability of the material upon further cycling.[8] In contrast, single-crystal (SC) NMC particles–consisting of continuous lattice domains free of grain boundaries–exhibit superior mechanical robustness relative to conventional PC analogs. While PC particles are prone to intergranular cracking under repeated cycling due to anisotropic lattice distortions, SC particles are often reported to remain largely unaffected by internal stresses associated with phase transitions. Instead of fracturing, SC particles accommodate lattice strain through reversible dislocation gliding, which helps preserve structural integrity over extended cycling.[21] This characteristic contributes to improved cycle life of batteries, as demonstrated in study by Qian at al.[22] Nevertheless, SC particles often deliver a lower initial capacity than PC particles due to their longer cation deintercalation pathways. At the same time, nickel-rich layered oxides, although capable of achieving high energy density, face persistent challenges with CEI stability. Instability at the CEI can trigger transition-metal dissolution, the development of surface reconstruction layers, and oxygen release.[23-25] These reactions give rise to gas evolution, voltage fade, and impedance growth, all of which curtail cell durability, particularly under high cut-off voltages. It is also

important to note that in full-cell configurations, the solid-electrolyte interphase (SEI) formed on graphite anodes exacerbates CEI–SEI crosstalk, which in turn accelerates undesirable side reactions and contributes to faster performance degradation.[26, 27] Therefore, stabilizing the CEI is indispensable for unlocking the full potential of nickel-rich SC cathodes.[28, 29] Addressing CEI instability and designing strategies to suppress harmful interfacial reactions are thus key steps toward achieving stable, high-performance, and long-lasting battery operation.

Surface modification strategies, including elementally tuned coatings and artificial interphases, have proven effective in suppressing interfacial degradation while maintaining favorable lithium-ion transport.[13, 30-32] In this work, we report a molten eutectic-assisted synthesis of SC NMC9055 followed by a NMC622 coating applied via hand-mixing versus evaporation-coating process. By introducing a nickel-lean surface layer, our approach is designed to mitigate undesirable interfacial reactions from a stable CEI and improve long-term electrochemical performance. Through comprehensive structural, chemical and electrochemical characterizations, as well as half-cell performance evaluation, we demonstrated enhanced capacity retention and cycling stability of coated SC NMCs, highlighting the critical role of CEI stabilization in advancing high-energy cathodes for next-generation LIBs.

METHODS

Material synthesis

To synthesize the NMC 9055 core particles, first we measured lithium acetate dihydrate ($C_2H_3LiO_2 \cdot 2H_2O$, Thermo-Fisher Scientific, 99%), nickel acetate tetrahydrate ($C_4H_6NiO_4 \cdot 4H_2O$, Sigma-Aldrich, 99%), manganese acetate tetrahydrate ($C_4H_6MnO_4 \cdot 4H_2O$, Sigma-Aldrich, 99%) and cobalt acetate tetrahydrate ($C_4H_6CoO_4 \cdot 4H_2O$, Sigma-Aldrich, 99%) into a metal cation molar

ratio of 1.0 Li : 0.9 Ni : 0.05 Mn : 0.05 Co. To account for lithium leaching during the annealing process, 0.2 mol excess lithium was added. All powders were ground in a mortar and pestle before poured into a small glass petri dish to be heated on a hot plate at 100 ˚C for around 5 minutes, stirring occasionally with a metal spatula until a homogenous dark teal gel formed. We then deposited the gel in an alumina boat for annealing. After annealing in an open-air tube furnace, at 300 ˚C for 5 hours, with a heating rate of 5 ˚C/min and natural cooling, we removed the hardened expanded mixture and ground it into powder before annealed in a tube furnace utilizing the temperature swing method under oxygen. The tube furnace temperature was raised to 1000 ˚C at 5 ˚C/min and held for 3 hours, lowered to 900 ˚C at 2 ˚C/min and held for 10 hours, then lowered to 300 ˚C at 2 ˚C/min, and finally cooled naturally. We ground the final product by hand, passed it through sieve #325, and stored it in a humidity controlled dry room (RH<0.1%).

To prepare the coated NMC9055 cores, we prepared another eutectic gel with a cation molar ratio of 1.2 Li : 0.6 Ni : 0.2 Mn : 0.2 Co, using the previously described process. We dissolved 1g 622 mixture in 10 mL DI water to produce the evaporation coating solution and mixed 6 drops of coating solution with 0.491g NMC9055 core particles in a glass vial and dried the mixture overnight in a vacuum oven. We hand mixed 0.5g NMC9055 core particles into remaining 622 eutectic gel while still on the hot plate until well mixed. We annealed both coated materials separately under air at 300 C for 5 hours, ground and annealed again at a steady temperature of 750 ˚C for 12 hours under oxygen, then sieved once more through sieve #325 (45 μm opening). Detailed process and parameters are summarized in **Figure S1** and **Table S1**.

Material preparation environment and quality control

All materials were prepared using a consistent and well-controlled experimental platform to ensure reproducibility and minimize environmental variability. Precursor handling and mixing were

performed under ambient air conditions. Pre-calcination was carried out by heating the eutectic mixture in an alumina crucible placed in a quartz tube within Thermofisher tube furnace, operated under air in a chemical hood. High-temperature annealing was performed by heating the ground powders in an alumina crucible housed in an alumina tube within Thermofisher tube furnace under oxygen atmosphere. Following annealing, both the core material (NMC9055) and the coated material (NMC9055/622) were stored in a humidity-controlled dry room (RH<1%) prior to sieving and subsequent characterization and coating process.

Coin cell assembly and testing

To assemble half coin cells from the pristine, hand-mixed and evaporation-coated materials, each cathode material was first mixed into a slurry along with carbon black (C-NERGY SUPER C65), 8 wt% polyvinylidene fluoride (PVDF, 5130 Solef) in solution in spread on aluminum foil, and punched into electrode discs. We made a slurry mixture with mass ratio of 0.9 active material : 0.05 carbon black : 0.05 PVDF by mass PVDF in NMP solution and adding trace amounts of NMP until the slurry was an ink-like consistency. The slurry was casted onto aluminum foil, dried overnight in a vacuum oven at 120 ˚C before being punched out into 14 mm diameter cathode disks. The active materials loading of each disk is around 3 mg/cm^2. The cells were assembled in an Ar-filled glove box, with Gen 2 electrolyte - 1.2M $LiPF_6$ in ethylene carbonate (EC): ethyl methyl carbonate (EMC) (3:7 v:v), lithium metal anode disk, and a Celgard 2325 tri-layer separator. We constructed several cells using the pristine, hand-mixed and evaporation coated cathode material. The half cells were tested at C/10 (1C = 185 mA/g) with two different voltage windows: 2.8 – 4.3 V and 2.8 – 4.7 V.

Material Characterization

Journal of Electrochemical Energy Conversion and Storage. Received October 03, 2025;
Accepted manuscript posted January 19, 2026. doi:10.1115/1.4070915

Pristine NMC 9055, evaporation coated, and manual coated particles were all observed under a Zeiss-MERLIN^{TM} field-emission scanning electron microscope (SEM) to view morphology and qualitatively measure particle size distribution, and energy dispersive X-ray spectroscopy (EDS) to confirm elemental composition and distribution on the particle surface. We further characterized the pristine and evaporation coated material with a Malvern Panalytical X'PERT X-Ray Diffractometer (XRD) with Cu Kα radiation at 45 kV and 40 mA. Transmission X-ray images were collected on pristine and aged cathode particles using the full-field transmission X-Rays microscope (TXM) at beam line 6-2c at Stanford Linear Accelerator Center-Stanford Synchrotron Radiation Lightsource (SLAC-SSRL). Aged cathodes were retrieved from cycled coin cells and washed with dimethyl carbonate solvent inside the Ar glovebox and dried before being vacuum sealed for sample transferring. The cathode materials were scrapped off from the electrode disk and transferred into thin-walled glass capillary tubes (Charles-Supper, OD=0.1 mm, wall thickness: 0.01 mm) to ensure a few particles exist in the view of interest. Projection images were acquired over a 180° rotation in 1° increments, with five projections averaged per angle and reference images taken every 30 angles. The binning factors for all images were set to be 2, resulting in a pixel size of 28 nm and a field-of-view of 33 μm. Two-dimensional X-ray absorption near-edge structure (2D XANES) images were collected over a range of energies around the Ni K-edge (8290–8501 eV) using a liquid nitrogen cooled double-Si (111) monochromator crystal. Scans were conducted approximately 40 eV below and 170 eV above the Ni K absorption edge, using step sizes of 5 eV before the edge, 0.5 eV near the edge, 2 eV immediately post-edge, and 10 eV in the extended X-ray absorption fine structure (EXAFS) region for normalization. Obtained data was processed using TXM Wizard, including reference correction, averaging, image jitter and

magnification correction, edge-jump filtering, and normalization. The processed data were subsequently analyzed and plotted to visualize the 2D XANES features.

RESULTS AND DISCUSSION

The eutectic synthesis leverages the concept of liquid/molten eutectic formation at room or elevated temperatures, which enables unform mixing of precursors down to the atomic level. Such homogeneous mixing further ensures controlled phase formation during subsequent high-temperature annealing.[33-35] In this work, eutectic synthesis using acetic precursors promoted the rapid formation of a uniform molten mixture at 100 ˚C. Upon heating to 1000 ˚C, fast ionic diffusion facilitated the phase formation of the nuclei. When the annealing temperature was subsequently lowered to 900 °C and held, crystal growth proceeded while preserving the morphology of the primary nuclei, driven by the combined effects of mass transport and Ostwald ripening.[36] As a result, octahedral single-crystal particles with sizes ranging from 3 to 5 μm were obtained (**Figure 1a**). The hand-mixed coating strategy, however, yielded particles with larger sizes and greater degrees of agglomeration (**Figure 1b**). Additionally, small amorphous and incomplete crystals were observed, likely due to the deposition of thick NMC622 layers arising from inhomogeneous hand-mixing and the excess amount of precursor eutectic mixture. The lower annealing temperatures applied for coating did not provide sufficient energy for complete crystal growth compared to the conditions used for primary particle formation. In contrast, evaporation-coated SC particles displayed sizes and morphologies similar to those of pristine SC NMCs (**Figure 1c**). The use of a more diluted precursor solution produced thinner and more uniform NMC622 surface coatings. Subsequent annealing at 750 °C promoted the formation of conformal surface coatings on the pristine SC particles. SEM zoomed-in images further highlighted these distinctions (**Figure 1d-f**). The surface of pristine SC NMC9055 exhibited some nano-sized

particles (**Figure 1d**), which represent primary particles yet to undergo growth into larger SCs. After hand-mixing with NMC622 precursors, the overall shape of the SC core particles was preserved (**Figure 1e**), but the average particle size increased, accompanied by isotropic lamellar structures and additional small particles—likely NMC622 primary particles formed from excess precursor loading. The presence of a thick liquid eutectic coating layer promoted uneven heat transfer during annealing at 750 °C. Because heat propagates from the outer coating inward, the octahedral shape of the SC cores induced non-uniform volume expansion during the boiling of the eutectic mixture, ultimately leading to fragmentation of the liquid layer into discrete smaller particles rather than a continuous conformal film. Non-uniform mixing further exacerbated this issue, resulting in uneven heat distribution and poor coating uniformity. By contrast, evaporation-coated SC NMC9055 samples exhibited smoother surfaces compared to pristine SCs, with no apparent formation of additional primary particle aggregates (**Figure 1f**). The controlled use of minimal amounts of liquid eutectic precursor, combined with gradual evaporation, produced a thin, conformal NMC622 coating layer. As shown in the particle size distribution in **Figure S2**, the hand-mixing coating method produced slightly larger particles in comparison with the evaporation coating method. It is worth noting that particles coated via evaporation exhibit no significant change in size relative to pristine particles. A schematic illustration of the distinct coating formation pathways for hand-mixing and evaporation-coating methods is provided in **Figure 2**.

Journal of Electrochemical Energy Conversion and Storage. Received October 03, 2025;
Accepted manuscript posted January 19, 2026. doi:10.1115/1.4070915

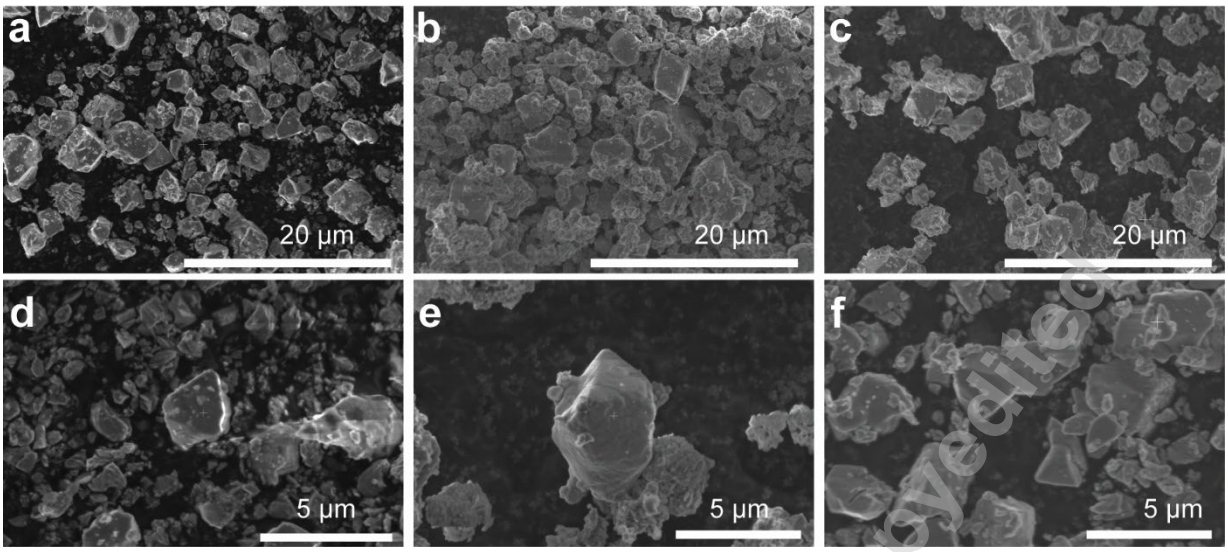

Figure 1. SEM images of pristine NMC9055 (a,d), hand-mixed NMC9055/622 (b,e) and evaporation coated NMC9055/622 (c,f).

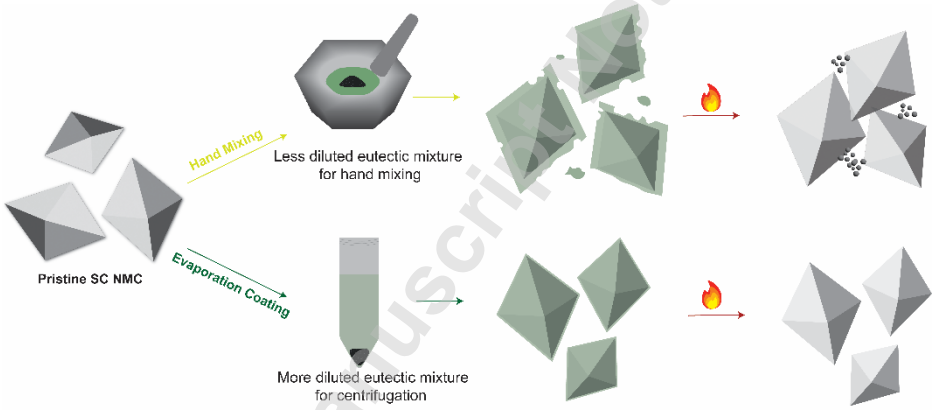

Figure 2. Schematic illustration of the coated SC NMCs with hand-mixing and evaporation-coating methods.

In addition to particle morphology, EDS elemental mappings were collected for each sample to evaluate the spatial distribution of transition metal elements on particle surfaces. As shown in **Figure 3a-d**, the distributions of Ni, Mn and Co appear uniform across the pristine SC particles, confirming the expected homogeneity of the bulk composition. After applying the hand-mixing coating process, however, regions of local inhomogeneity became evident in the elemental maps (circled in **Figure 3e-h**). This non-uniformity can be attributed to the deposition of a

Journal of Electrochemical Energy Conversion and Storage. Received October 03, 2025;
Accepted manuscript posted January 19, 2026. doi:10.1115/1.4070915

relatively thick eutectic mixture layer on the SC particle surfaces prior to annealing. The poor thermal conductivity of such a thick surface layer may hinder efficient heat transfer during annealing, which in turn promotes aggressive bubbling and the development of non-linear thermal gradients. These localized instabilities accelerate the breakdown of the eutectic mixture and ultimately result in the formation of discrete secondary primary particles, rather than a smooth conformal coating. In contrast, the evaporation coating process begins with a dilute eutectic solution that enables homogeneous wetting and intimate contact between the precursor species and the NMC9055 particle surfaces. This uniform precursor distribution promotes more even thermal treatment during annealing, facilitating controlled interdiffusion and reaction at the particle surface. As a result, the annealed particles retain a uniform distribution of transition-metal elements across the entire area of interest, as evidenced by the EDS maps in **Figure 3i–l**. These results underscore the importance of the coating strategy and precursor distribution, together with thermal transport during annealing, in governing the final surface-engineered particle morphology and homogeneity.

Journal of Electrochemical Energy Conversion and Storage. Received October 03, 2025;
Accepted manuscript posted January 19, 2026. doi:10.1115/1.4070915

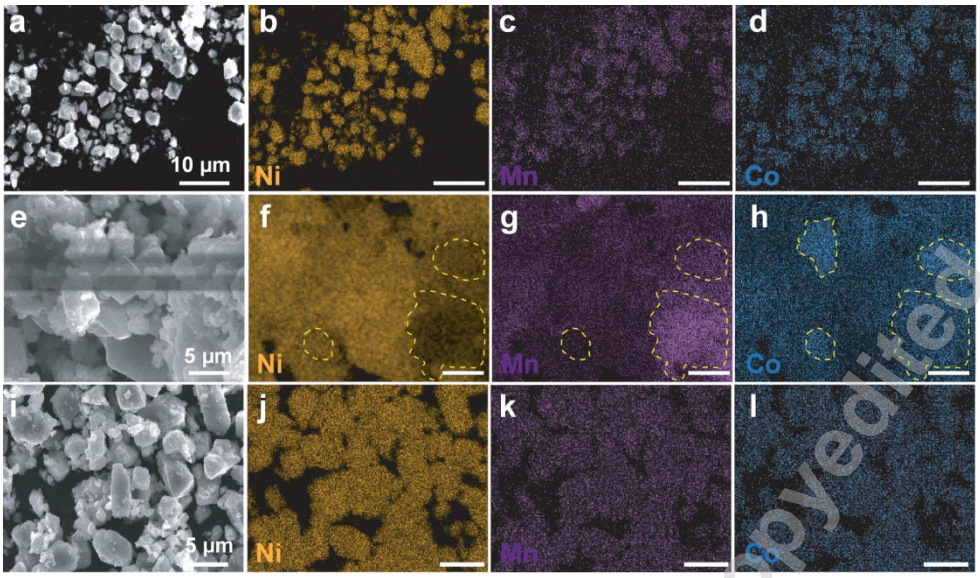

Figure 3. SEM images and EDS elemental mapping results of (a)-(d) pristine NMC9055, and cathode particles with coating by (e)-(h) hand-mixing method, and (i)-(l) evaporation method. Scale bars in (b–d), (f–h), and (j–l) are identical to those in (a), (e), and (i), respectively.

To further confirm the structural phases of these materials, XRD patterns of the pristine and the coated samples were compared in **Figure 4**. The pristine SC NMC9055 exhibited the expected R-3m hexagonal layered structure (**Figure 4a**).[37] To assess the degree of cation mixing, the intensity ratio between the (003) and (104) reflections was calculated.[38] The $I_{(003)}/I_{(104)}$ values were found to be 1.27 for pristine SC NMC9055, 1.53 for the hand-mixing coated, and 1.15 for evaporation-coatedNMC9055s. For the hand-mixed NMC9055/622, peak broadening was observed (**Figure 4b**). The larger full width at half maximum (FWHM) values for XRD peaks are consistent with the presence of smaller, less well-ordered crystallites, in agreement with SEM observations that revealed irregular particle agglomerates and incomplete crystal growth. The evaporation-coated NMC9055/622 exhibited only a slightly higher cation mixing level compared to pristine particles (**Figure 4c**), while maintaining well-defined layered reflections and without evidence of phase separation. The slightly increased cation mixing observed in the evaporation-coated material may arise from the prolonged immersion of NMC9055 in the diluted eutectic

Journal of Electrochemical Energy Conversion and Storage. Received October 03, 2025;
Accepted manuscript posted January 19, 2026. doi:10.1115/1.4070915

mixture of acetate-based NMC622 precursors during the coating and drying process, which caused partial lithium dissolution compared to the relatively rapid hand-mixing approach. In contrast, although the hand-mixed coated material exhibits a comparable or higher level of cation mixing, its XRD peaks are noticeably broader than those of the pristine material or the evaporation-coated sample. This additional broadening is likely attributable to inhomogeneous mixing between the NMC622 precursors and NMC9055, leading to the formation of smaller NMC622 crystallites aside from NMC9055 upon annealing rather than a more uniform surface layer on top of NMC9055. Taken together, SEM and XRD characterizations indicate that the evaporation-coating strategy yields SC particles with more desirable engineered surface, including smoother morphology, controlled particle size, and improved crystallinity, while avoiding the drawbacks of inhomogeneity and secondary particle formation observed in coated NMCs by hand-mixing. Based

Journal of Electrochemical Energy Conversion and Storage. Received October 03, 2025;
Accepted manuscript posted January 19, 2026. doi:10.1115/1.4070915

on these advantages, the electrochemical performance of the evaporation-coated samples was subsequently evaluated in comparison with pristine SC NMC9055.

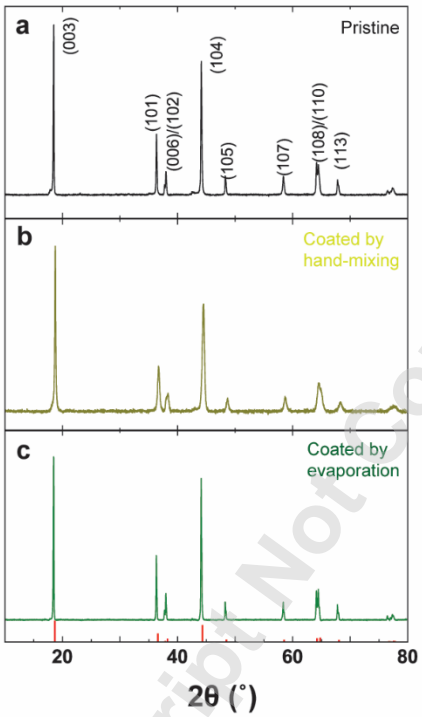

Figure 4. XRD of (a) pristine NMC9055 particles, (b) NMC9055/622 particles enabled by hand-mixing, and (c) NMC9055/622 particles enabled by evaporation coating. (Reference of O3-type layered structure was indicated with red lines at the bottom)

Galvanostatic charge/discharge profiles and cycling performance of pristine and evaporation-coated NMC9055s are compared in **Figure 5**. Baseline surface chemistry of the pristine cathode was established by XPS (**Figure S3**), while the impact of surface modification on CEI stability is assessed through electrochemical performance metrics that sensitively reflect interfacial degradation processes during cycling. Evaporation-coated SCs showed an initial reversible capacity of 10% more than pristine SC NMC9055 at 0.1 C within 2.8-4.3 V. The capacity retention of coated cathodes is 66% after 130 cycles, which is higher than 51% of pristine cathodes. The initial Coulombic efficiencies (CEs) of coated versus uncoated cathodes are 80% and 77%,

respectively. The improvement in initial CE demonstrated an improved CEI due to the coating layer. The increased reversibly capacity of coated cathodes can be correlated to improved electrochemical redox activities due to the formation of a stable, ionically more conductive CEI. When ramping up the cutoff voltage from 4.3 to 4.7 V, higher initial reversible capacity was realized for both uncoated and coated cathodes, to 160 and 174 mAh/g, respectively. The unusual fluctuations in charge/discharge capacities were a result of temporary power outages. The coated and uncoated cathodes demonstrated 80% and 70% of capacity retention at 98th cycle. It is worth noticing that after the power-outage induced capacity fluctuations, both cells were able to recover the reversible capacities and continue for more than 150 cycles. The coated cathodes maintained similar capacity retention even when being cycled in a wider voltage range. The stable CEI not only enabled stable cycling performance with higher capacity retention but also ensured minimum side reactions that cause fast capacity fading at higher cutoff voltage, further highlighting the stability of the coated cathodes against the liquid electrolyte. Future work may improve evaporation-coated materials by shortening the immersion time or incorporating additional excess amount of lithium in the NMC622 eutectic mixture to reduce cation mixing and further improve cycling stability.

Journal of Electrochemical Energy Conversion and Storage. Received October 03, 2025;
Accepted manuscript posted January 19, 2026. doi:10.1115/1.4070915

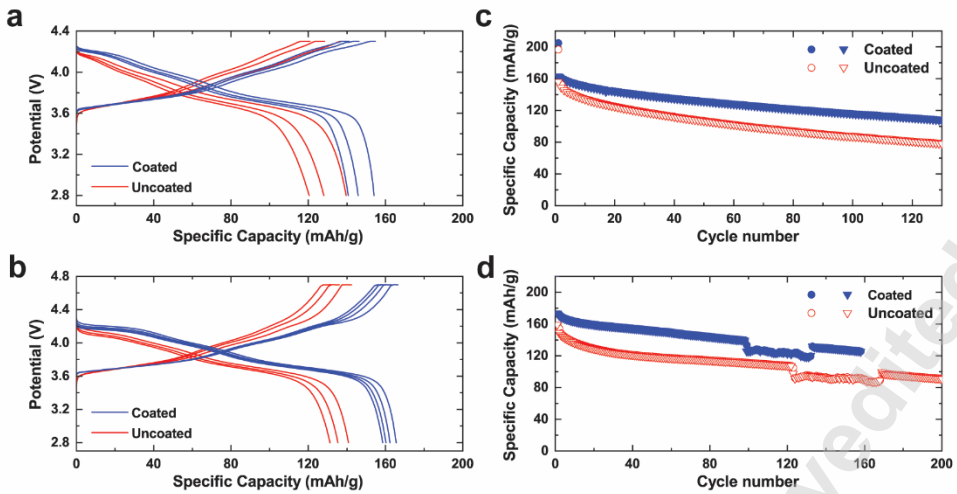

Figure 5. (a) Galvanostatic charge/discharge curves and (b) cycling plot of pristine and coated SC NMC9055 cathodes in half cells cycled at 0.1C between 2.8 – 4.3 V; (c) Galvanostatic charge/discharge curves and (b) cycling plot of pristine and coated SC NMC9055 cathodes in half cells cycled at 0.1C between 2.8 – 4.7 V.

2D-XANES analysis was carried out at SSRL to assess the Ni redox behavior of coated and uncoated single-crystal cathode particles. The resulting 2D maps and corresponding Ni absorption edge distributions are shown in **Figure 6**. As expected, the absorption edge position is strongly correlated with the Ni oxidation state, with higher oxidation states (Ni^{3+}/Ni^{4+}) corresponding to higher relative energies compared to reduced Ni^{2+}. During charging, delithiation of the layered oxide drives oxidation of Ni, observed as a systematic shift of the edge to higher energies across the particle domains. Conversely, lithiation during discharge reduces Ni and shifts the edge toward lower energies. The pristine uncoated particle displays a uniform edge-energy distribution, suggesting a homogeneous composition prior to cycling (**Figure 6a**). The most pronounced differences emerge upon discharge: while the uncoated particle (**Figure 6b**) displays significant spatial heterogeneity and incomplete reduction, the coated particle (**Figure 6c**) exhibits a homogeneous distribution of edge energies, indicative of uniform and highly reversible lithiation. These observations directly link the improved cycling stability of the coated material to its more

reversible and uniform Ni redox behavior, which enhances coulombic efficiency and underpins superior long-term performance.

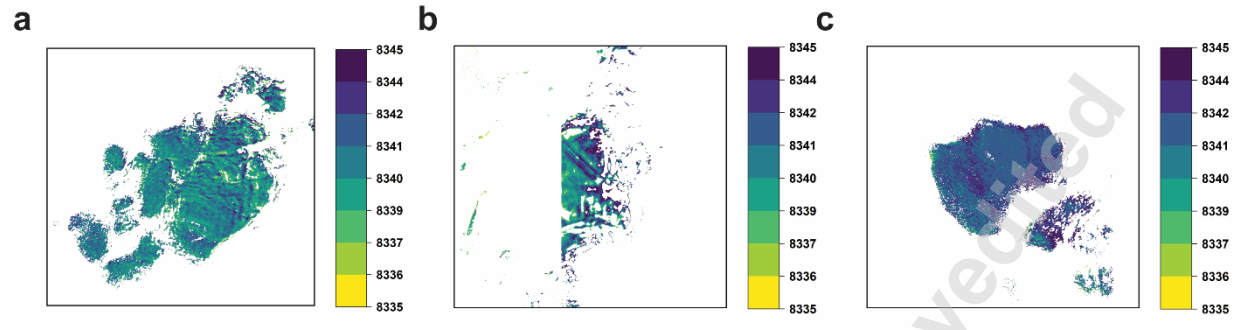

Figure 6. TXM of Ni K-edge 2D XANES Map of (a) uncoated pristine NMC9055, (b) uncoated pristine NMC9055 at fully discharged state, (c) coated NMC9055 at fully discharged state. (The panel size is 33 µm by 33 µm)

CONCLUSION

In this study, we demonstrated that surface engineering of SC NMC9055 via a nickel-lean NMC622 coating prepared by eutectic-assisted evaporation yields notable improvements in electrochemical performance compared to pristine counterparts. Structural and morphological analyses confirmed that the evaporation coating forms a uniform and conformal surface layer, mitigating the issues of inhomogeneity and agglomeration seen with hand-mixed coatings. Electrochemical testing revealed that the coated SCs exhibited higher initial reversible capacity, improved coulombic efficiency, and enhanced capacity retention, even under extended cycling and higher cut-off voltages. Moreover, synchrotron-based 2D XANES mapping results indicated that the improved stability originates from more uniform and reversible Ni redox behavior, demonstrating that the engineered surface layer effectively stabilizes the CEI and suppresses degradation pathways. Looking forward, these results underscore the importance of rationally designed surface modification strategies to unlock the full potential of Ni-rich SC cathodes. Ultimately, scalable coating methods that enhance CEI stability while preserving high energy

density will play a pivotal role in enabling durable, safe, and cost-effective lithium-ion batteries for both electric vehicles and grid-scale storage applications.

ACKNOWLEDGMENTS

This research at Oak Ridge National Laboratory, managed by UT Battelle, LLC, for the US Department of Energy (DOE) under contract DE-AC05-00OR22725, was supported by the Assistant Secretary for Energy Efficiency and Renewable Energy, Office of Vehicle Technologies of the US Department of Energy through Cathode Electrolyte Interphase Consortium. Collin Farrell was supported in part by the U.S. Department of Energy, Office of Science, Office of Workforce Development for Teachers and Scientists (WDTS) under the Science Undergraduate Laboratory Internships (SULI) program. Use of the Stanford Synchrotron Radiation Lightsource, SLAC National Accelerator Laboratory, is supported by the U.S. Department of Energy, Office of Science, Office of Basic Energy Sciences under contract DE-AC02–76SF00515.

CONFLICT OF INTEREST

The authors declare no conflict of interest.

REFERENCES

(1) Ank, M.; Sommer, A.; Gamra, K. A.; Schöberl, J.; Leeb, M.; Schachtl, J.; Streidel, N.; Stock, S.; Schreiber, M.; Bilfinger, P. Lithium-ion cells in automotive applications: Tesla 4680 cylindrical cell teardown and characterization. *J. Electrochem. Soc.* **2023**, *170* (12), 120536.
(2) Reza, M.; Mannan, M.; Mansor, M.; Ker, P. J.; Mahlia, T. I.; Hannan, M. Recent advancement of remaining useful life prediction of lithium-ion battery in electric vehicle applications: A review of modelling mechanisms, network configurations, factors, and outstanding issues. *Energy Reports* **2024**, *11*, 4824-4848.
(3) Verma, A.; Saikia, T.; Saikia, P.; Rakshit, D.; Ugalde-Loo, C. E. Thermal performance analysis and experimental verification of lithium-ion batteries for electric vehicle applications through optimized inclined mini-channels. *Applied Energy* **2023**, *335*, 120743.
(4) Wang, L.; Chen, B.; Ma, J.; Cui, G.; Chen, L. Reviving lithium cobalt oxide-based lithium secondary batteries-toward a higher energy density. *Chem. Soc. Rev.* **2018**, *47* (17), 6505-6602.
(5) Kalluri, S.; Yoon, M.; Jo, M.; Park, S.; Myeong, S.; Kim, J.; Dou, S. X.; Guo, Z.; Cho, J. Surface engineering strategies of layered LiCoO2 cathode material to realize high-energy and high-voltage Li-ion cells. *Adv. Energy Mater.* **2017**, *7* (1), 1601507.
(6) Pang, P.; Wang, Z.; Tan, X.; Deng, Y.; Nan, J.; Xing, Z.; Li, H. LiCoO2@ LiNi0. 45Al0. 05Mn0. 5O2 as high-voltage lithium-ion battery cathode materials with improved cycling performance and thermal stability. *Electrochim. Acta* **2019**, *327*, 135018.
(7) Zhao, S.; Guo, Z.; Yan, K.; Wan, S.; He, F.; Sun, B.; Wang, G. Towards high-energy-density lithium-ion batteries: Strategies for developing high-capacity lithium-rich cathode materials. *Energy Storage Mater.* **2021**, *34*, 716-734.
(8) Camargos, P. H.; dos Santos, P. H.; dos Santos, I. R.; Ribeiro, G. S.; Caetano, R. E. Perspectives on Li-ion battery categories for electric vehicle applications: a review of state of the art. *Int. J. Energy Res.* **2022**, *46* (13), 19258-19268.
(9) Frith, J. T.; Lacey, M. J.; Ulissi, U. A non-academic perspective on the future of lithium-based batteries. *Nat. Commun.* **2023**, *14* (1), 420.
(10) Ma, L.; Nie, M.; Xia, J.; Dahn, J. A systematic study on the reactivity of different grades of charged Li [NixMnyCoz] O2 with electrolyte at elevated temperatures using accelerating rate calorimetry. *J. Power Sources* **2016**, *327*, 145-150.
(11) Choi, J.; Dong, L.; Yu, C.-Y.; O'Meara, C.; Lee, E.; Kim, J.-H. Relationship of chemical composition and moisture sensitivity in LiNi x Mn y Co1− X− Y O2 for lithium-ion batteries. *J. Electrochem. En. Conv. Stor.* **2021**, *18* (4), 041009.
(12) Das, D.; Manna, S.; Puravankara, S. Electrolytes, additives and binders for NMC cathodes in Li-Ion batteries—A review. *Batteries* **2023**, *9* (4), 193.
(13) Kaur, G.; Gates, B. D. Surface coatings for cathodes in lithium ion batteries: from crystal structures to electrochemical performance. *J. Electrochem. Soc.* **2022**, *169* (4), 043504.
(14) Tang, B.; Zhang, N.; Alter, E.; Eldesoky, A.; Dahn, J. Transition metal dissolution from single crystal Li [Ni1− x− yMnxCoy] O2 and Li [Ni1− xMnx] O2 positive electrodes subjected to aggresive conditions. *J. Electrochem. Soc.* **2024**, *171* (1), 010518.
(15) Tanim, T. R.; Yang, Z.; Finegan, D. P.; Chinnam, P. R.; Lin, Y.; Weddle, P. J.; Bloom, I.; Colclasure, A. M.; Dufek, E. J.; Wen, J. A comprehensive understanding of the aging effects of extreme fast charging on high Ni NMC cathode. *Adv. Energy Mater.* **2022**, *12* (22), 2103712.
(16) Liu, Z.; Zhang, J.; Luo, J.; Guo, Z.; Jiang, H.; Li, Z.; Liu, Y.; Song, Z.; Liu, R.; Liu, W.-D. Approaching ultimate synthesis reaction rate of Ni-rich layered cathodes for lithium-ion batteries. *Nano-Micro Letters* **2024**, *16* (1), 210.

(17) Li, P.-Y.; Huang, Y.-D.; Luo, Y.-H.; Wei, H.-X.; Luo, R.; Tang, L.-B.; Chen, H.-Z.; Zhang, X.-H.; Zheng, J.-C. Decoding Li+/H+ ion exchange route toward low-temperature synthesis of layered oxide cathode materials for lithium-ion batteries. *Rare Metals* **2024**, *43* (12), 6329-6339.
(18) Akhilash, M.; Salini, P.; John, B.; Mercy, T. A journey through layered cathode materials for lithium ion cells–from lithium cobalt oxide to lithium-rich transition metal oxides. *J. Alloys Compd.* **2021**, *869*, 159239.
(19) Wang, C.; Zhao, H.; Wang, J.; Wang, J.; Lv, P. Electrochemical performance of modified artificial graphite as anode material for lithium ion batteries. *Ionics* **2013**, *19* (2), 221-226.
(20) Houache, M. S.; Yim, C.-H.; Karkar, Z.; Abu-Lebdeh, Y. On the current and future outlook of battery chemistries for electric vehicles—mini review. *Batteries* **2022**, *8* (7), 70.
(21) Bi, Y.; Tao, J.; Wu, Y.; Li, L.; Xu, Y.; Hu, E.; Wu, B.; Hu, J.; Wang, C.; Zhang, J.-G. Reversible planar gliding and microcracking in a single-crystalline Ni-rich cathode. *Science* **2020**, *370* (6522), 1313-1317.
(22) Qian, G.; Zhang, Y.; Li, L.; Zhang, R.; Xu, J.; Cheng, Z.; Xie, S.; Wang, H.; Rao, Q.; He, Y. Single-crystal nickel-rich layered-oxide battery cathode materials: synthesis, electrochemistry, and intra-granular fracture. *Energy Storage Mater.* **2020**, *27*, 140-149.
(23) Jung, R.; Linsenmann, F.; Thomas, R.; Wandt, J.; Solchenbach, S.; Maglia, F.; Stinner, C.; Tromp, M.; Gasteiger, H. A. Nickel, manganese, and cobalt dissolution from Ni-rich NMC and their effects on NMC622-graphite cells. *J. Electrochem. Soc.* **2019**, *166* (2), A378-A389.
(24) Teichert, P.; Eshetu, G. G.; Jahnke, H.; Figgemeier, E. Degradation and aging routes of Ni-rich cathode based Li-ion batteries. *Batteries* **2020**, *6* (1), 8.
(25) Jung, R.; Metzger, M.; Maglia, F.; Stinner, C.; Gasteiger, H. A. Oxygen release and its effect on the cycling stability of LiNixMnyCozO2 (NMC) cathode materials for Li-ion batteries. *J. Electrochem. Soc.* **2017**, *164* (7), A1361.
(26) Kühn, S. P.; Edström, K.; Winter, M.; Cekic-Laskovic, I. Face to face at the cathode electrolyte interphase: from interface features to interphase formation and dynamics. *Adv. Mater. Interfaces* **2022**, *9* (8), 2102078.
(27) Sahore, R.; Dogan, F.; Bloom, I. D. Identification of electrolyte-soluble organic cross-talk species in a lithium-ion battery via a two-compartment cell. *Chem. Mater.* **2019**, *31* (8), 2884-2891.
(28) Shadike, Z.; Chen, Y.; Hu, E.; Zhang, J.; Yang, X.-Q. Interphasial engineering for Ni-rich NMC cathode materials. *Trends Chem.* **2023**, *5* (10), 775-787.
(29) Xiao, J.; Adelstein, N.; Bi, Y.; Bian, W.; Cabana, J.; Cobb, C. L.; Cui, Y.; Dillon, S. J.; Doeff, M. M.; Islam, S. M. Assessing cathode–electrolyte interphases in batteries. *Nat. Energy* **2024**, *9* (12), 1463-1473.
(30) Liang, L.; Zhang, W.; Zhao, F.; Denis, D. K.; Zaman, F. U.; Hou, L.; Yuan, C. Surface/interface structure degradation of Ni-rich layered oxide cathodes toward lithium-ion batteries: fundamental mechanisms and remedying strategies. *Adv. Mater. Interfaces* **2020**, *7* (3), 1901749.
(31) Awasthi, S.; Moharana, S.; Kumar, V.; Wang, N.; Chmanehpour, E.; Sharma, A. D.; Tiwari, S. K.; Kumar, V.; Mishra, Y. K. Progress in doping and crystal deformation for polyanions cathode based lithium-ion batteries. *Nano Materials Science* **2024**, *6* (5), 504-535.
(32) Ahaliabadeh, Z.; Miikkulainen, V.; Mäntymäki, M.; Colalongo, M.; Mousavihashemi, S.; Yao, L.; Jiang, H.; Lahtinen, J.; Kankaanpää, T.; Kallio, T. Stabilized Nickel-Rich-Layered Oxide Electrodes for High-Performance Lithium-Ion Batteries. *Energy & Environmental Materials* **2024**, *7* (6), e12741.

(33) Li, M.; Wood, D. L.; Bai, Y.; Essehli, R.; Amin, M. R.; Jafta, C.; Muralidharan, N.; Li, J.; Belharouak, I. Eutectic synthesis of the P2-type Na x Fe1/2Mn1/2O2 cathode with improved cell design for sodium-ion batteries. *ACS Appl. Mater. Interfaces* **2020**, *12* (21), 23951-23958.
(34) Li, M.; Jafta, C. J.; Geng, L.; Liu, J.; Bai, Y.; Li, J.; Essehli, R.; Belharouak, I. Correlation of oxygen anion redox activity to in-plane honeycomb cation ordering in naxniymn1− yo2 cathodes. *Adv. Energy Sustain. Res.* **2022**, *3* (7), 2200027.
(35) Hawley, W. B.; Li, M.; Li, J. Room-temperature eutectic synthesis for upcycling of cathode materials. *Batteries* **2023**, *9* (10), 498.
(36) Wang, T.; Ren, K.; He, M.; Dong, W.; Xiao, W.; Pan, H.; Yang, J.; Yang, Y.; Liu, P.; Cao, Z. Synthesis and manipulation of single-crystalline lithium nickel manganese cobalt oxide cathodes: A review of growth mechanism. *Front. Chem.* **2020**, *8*, 747.
(37) Hwang, S.; Kim, S. M.; Bak, S.-M.; Kim, S. Y.; Cho, B.-W.; Chung, K. Y.; Lee, J. Y.; Stach, E. A.; Chang, W. Using real-time electron microscopy to explore the effects of transition-metal composition on the local thermal stability in charged Li x Ni y Mn z Co1–y–z O2 cathode materials. *Chem. Mater.* **2015**, *27* (11), 3927-3935.
(38) Zhang, X.; Jiang, W.; Mauger, A.; Gendron, F.; Julien, C. Minimization of the cation mixing in Li1+ x (NMC) 1− xO2 as cathode material. *J. Power Sources* **2010**, *195* (5), 1292-1301.

Journal of Electrochemical Energy Conversion and Storage. Received October 03, 2025;
Accepted manuscript posted January 19, 2026. doi:10.1115/1.4070915

Supplementary Information

Stabilizing Cathode–Electrolyte Interphase of Nickel-Rich Single-Crystal Cathodes for Lithium-Ion Batteries

Collin Farrell,[1] Marm Dixit,[1] Molleigh Preefer,[2] Ritu Sahore,[3] Saiful M. Islam,[4] Subrata Chandra Roy,[4] Mengya Li*[1]

1 Electrification and Energy Infrastructure Division, Oak Ridge National Laboratory, Oak Ridge, Tennessee 37831, USA

2 Stanford Synchrotron Radiation Lightsource, SLAC National Accelerator Laboratory, Menlo Park, CA 94025, USA

3 Chemical Sciences Division, Oak Ridge National Laboratory, Oak Ridge, Tennessee 37830, USA

4 Department of Chemistry, Physics, and Atmospheric Sciences, Jackson State University, Jackson, Mississippi 39217, USA

***Corresponding author:**

Mengya Li (lim1@ornl.gov)

Journal of Electrochemical Energy Conversion and Storage. Received October 03, 2025;
Accepted manuscript posted January 19, 2026. doi:10.1115/1.4070915

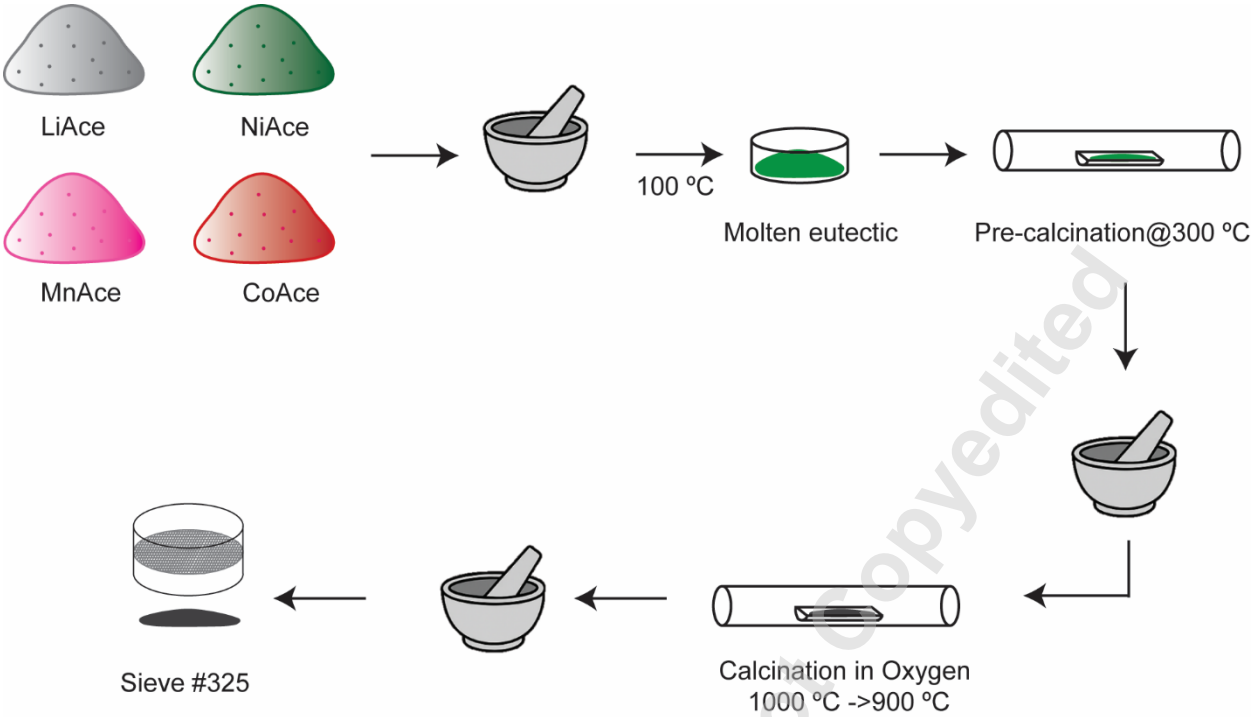

Figure S1. Flowchart of the eutectic synthesis of single-crystal NMC9055.

Table S1. Synthesis parameters of core material (NMC9055) and shell material (NMC622).

Step	Material	Molar Ratio (mol)				Calcination temperature (˚C)	
		Li	Ni	Mn	Co	Pre-calcination	High-T annealing
Core synthesis	NMC9055	1.0 (+ 0.2 excess)	0.9	0.05	0.05	300	1000->900
Coating (shell)	NMC622	1.0 (+ 0.2 excess)	0.6	0.2	0.2	300	750

Journal of Electrochemical Energy Conversion and Storage. Received October 03, 2025;
Accepted manuscript posted January 19, 2026. doi:10.1115/1.4070915

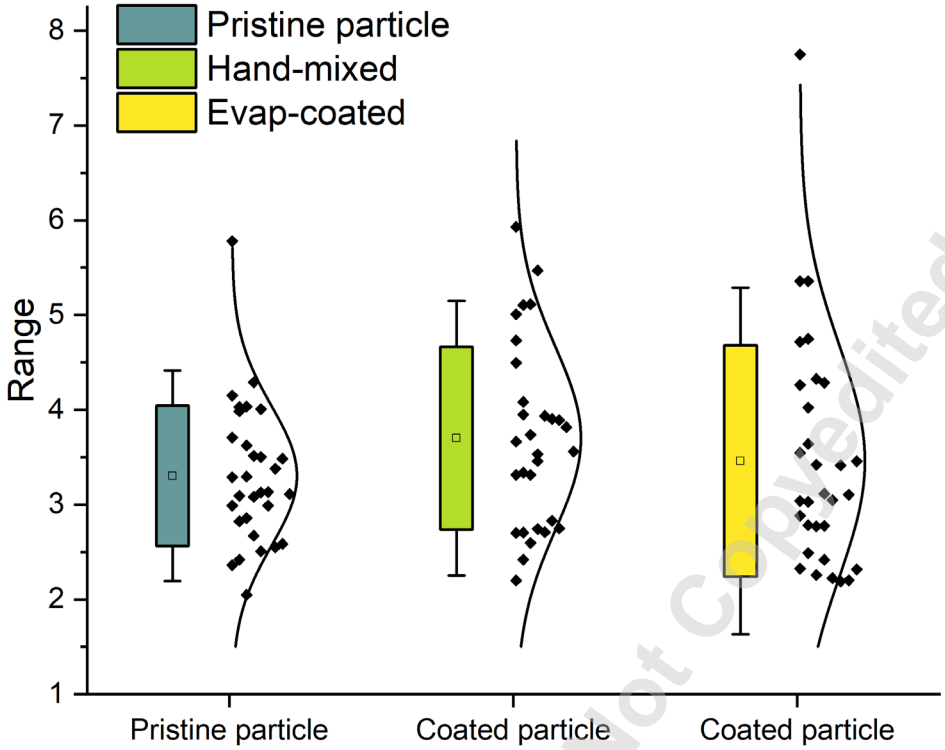

Figure S2. Particle size distribution of pristine, coated particle (hand-mixed) and coated (evap-coated) with average size of: 3.31, 3.70 and 3.46 µm, respectively.

Journal of Electrochemical Energy Conversion and Storage. Received October 03, 2025;
Accepted manuscript posted January 19, 2026. doi:10.1115/1.4070915

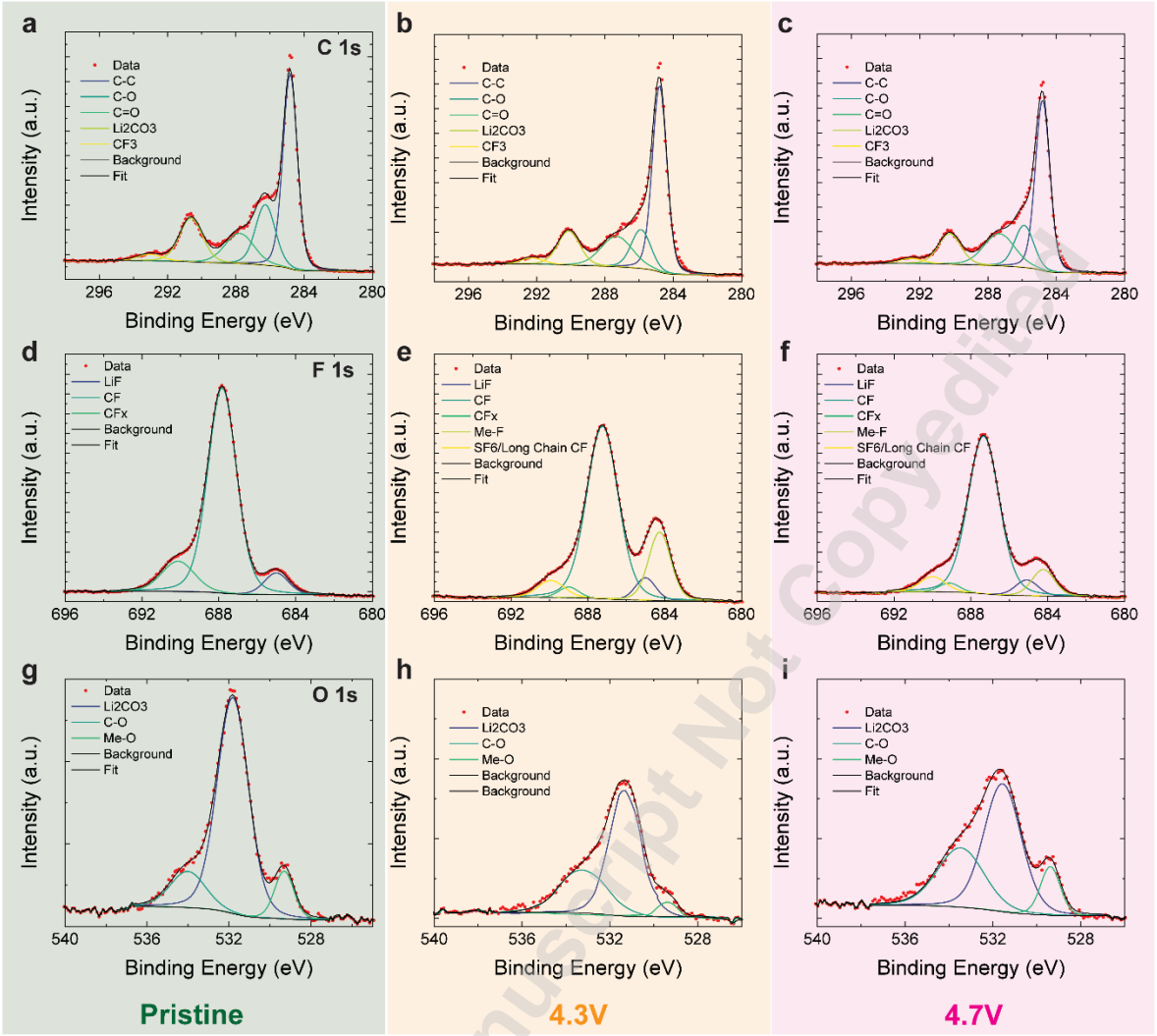

Figure S3. X-ray photoelectron spectroscopy results of (a-c) C 1s, (d-f) F 1s, (g-i) O 1s spectra of NMC9055 at pristine, charged to 4.3V and charged to 4.7V states.